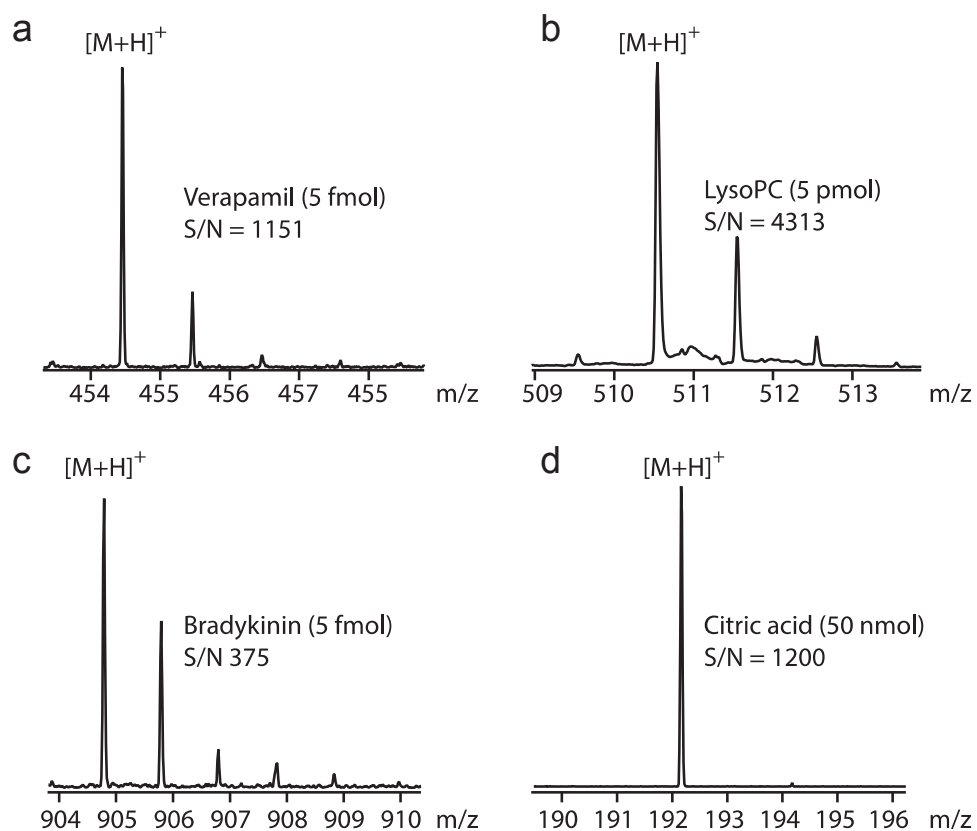
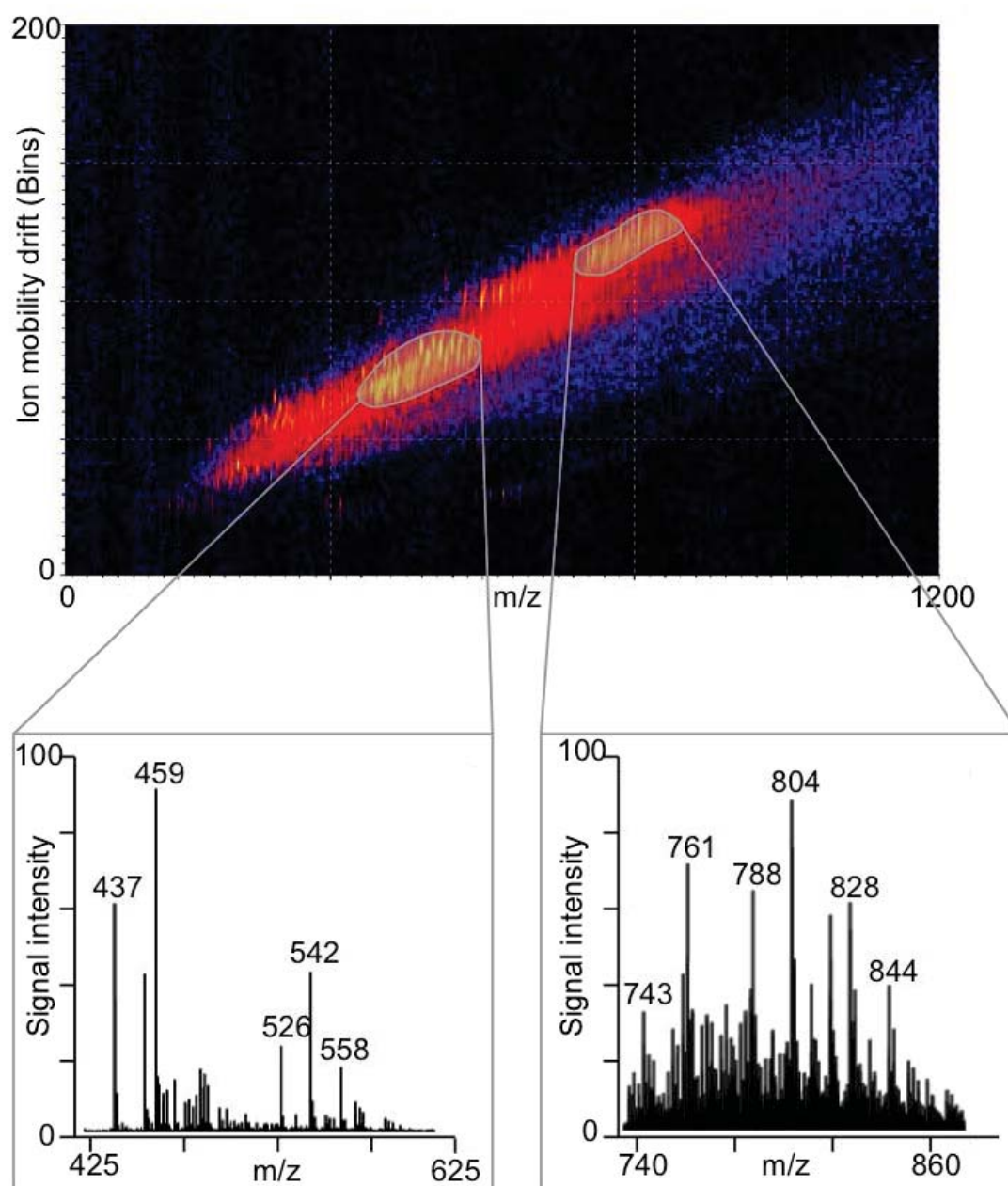


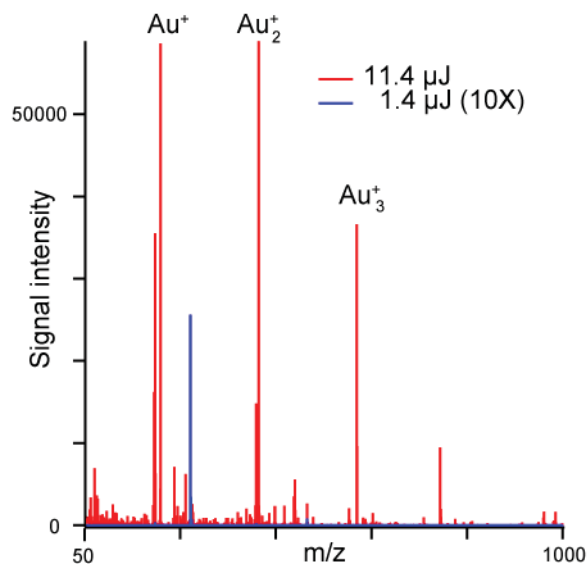
Supplementary Figures



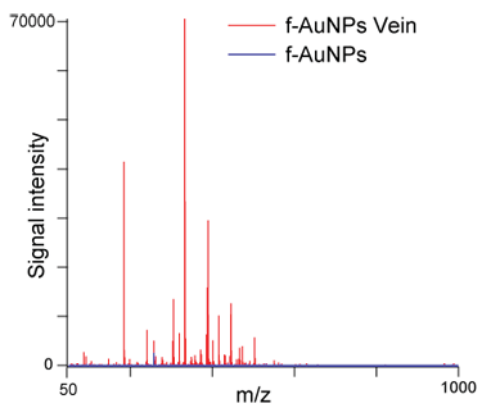
Supplementary Figure 1. Mass spectra collected using fluorinated gold nanoparticles. **(a)** Detection of a drug (verapamil), **(b)** endogenous metabolite (lysoPC), and **(c)** peptide (bradykinin) in positive ionization mode and **(d)** endogenous metabolite (citric acid) in negative ionization mode.



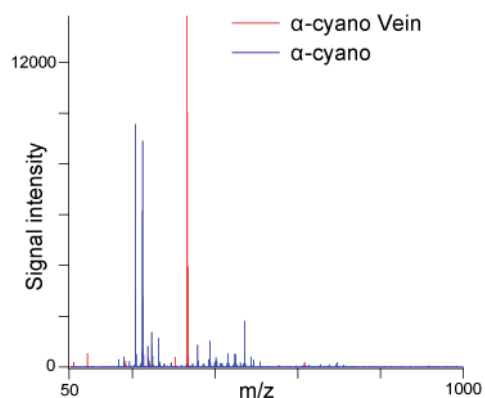
Supplementary Figure 2. Characterization of complex plasma extraction using ion mobility-MS with fluorinated AuNPs, and the representative mass spectrum in the mass range 420-600 and 740-870 Da.



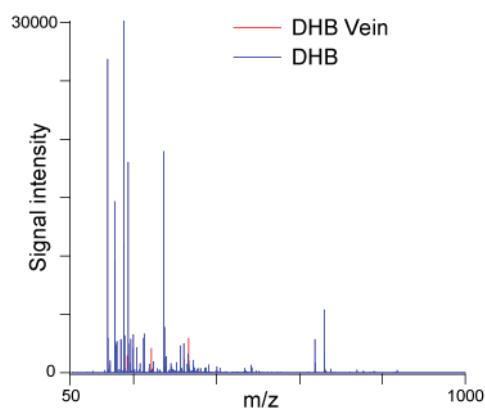
Supplementary Figure 3. Generation of gold clusters at high laser energy. The red spectrum shows the gold clusters formed at high laser energy (11.4 μJ) and the overlaid blue spectrum shows the background generated at the typical operating energy (1.4 μJ).



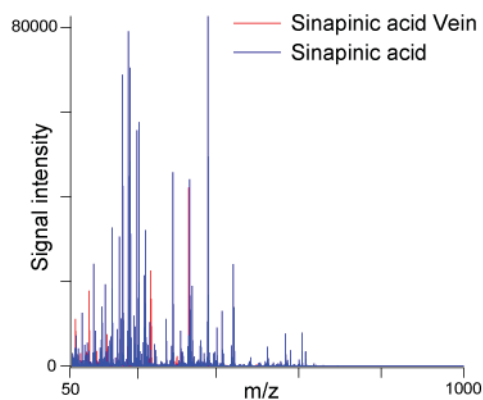
Supplementary Figure 4. F-AuNP background signal compared to tissue signal: vein. The red spectrum shows the signal intensities generated from f-AuNP coated vein and the overlaid blue spectrum shows the background generated at the typical operating energy (1.4 μJ).



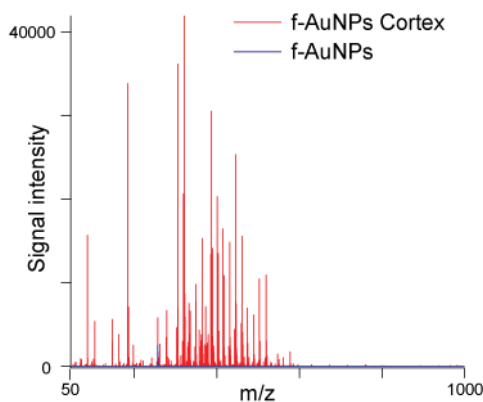
Supplementary Figure 5. α -cyano-4-hydroxycinnamic acid (α -cyano) background signal compared to tissue signal: vein. The red spectrum shows the signal intensities generated from f-AuNP coated vein and the overlaid blue spectrum shows the background generated at the typical operating energy (6.5 μ J).



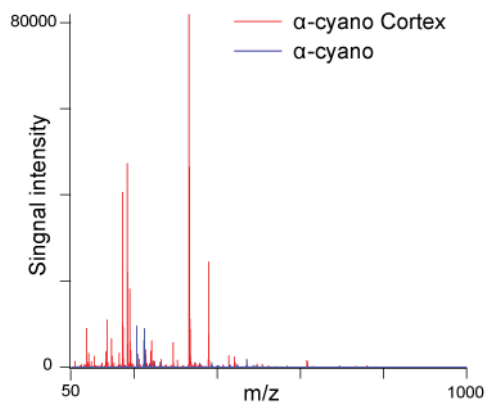
Supplementary Figure 6. 2,5-dihydroxybenzoic acid (DHB) background signal compared to tissue signal: vein. The red spectrum shows the signal intensities generated from f-AuNP coated vein and the overlaid blue spectrum shows the background generated at the typical operating energy (6.5 μ J).



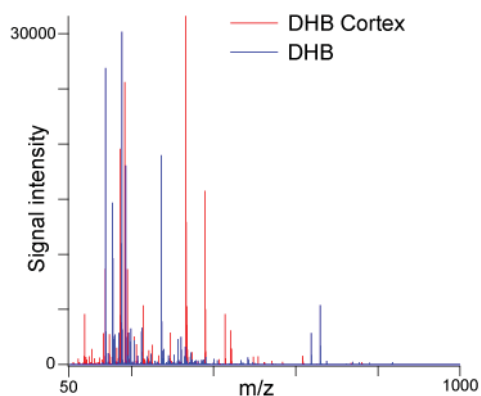
Supplementary Figure 7. Sinapinic acid background signal compared to tissue signal: vein. The red spectrum shows the signal intensities generated from f-AuNP coated vein and the overlaid blue spectrum shows the background generated at the typical operating energy (6.5 μJ).



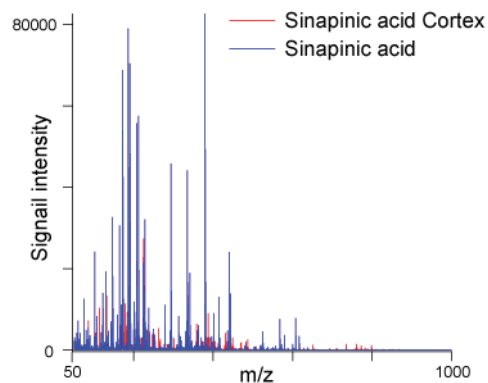
Supplementary Figure 8. F-AuNP background signal compared to tissue signal: mouse cerebral cortex. The red spectrum shows the signal intensities generated from f-AuNP coated cortex and the overlaid blue spectrum shows the background generated at the typical operating energy (1.4 μJ).



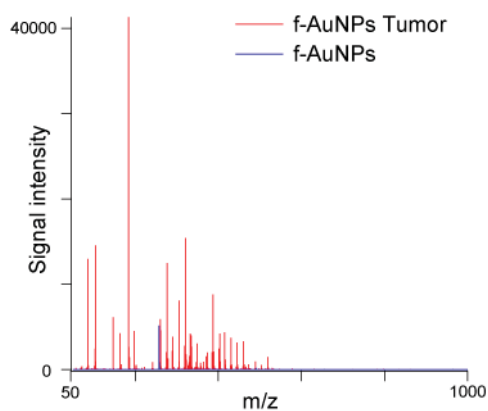
Supplementary Figure 9. α-cyano-4-hydroxycinnamic acid (α-cyano) background signal compared to tissue signal: mouse cerebral cortex. The red spectrum shows the signal intensities generated from f-AuNP coated cortex and the overlaid blue spectrum shows the background generated at the typical operating energy (6.5 μJ).



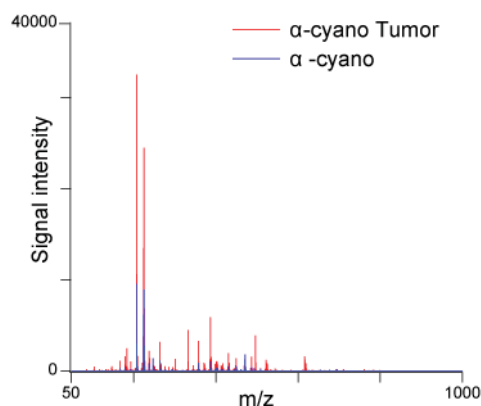
Supplementary Figure 10. 2,5-dihydroxybenzoic acid (DHB) background signal compared to tissue signal: mouse cerebral cortex. The red spectrum shows the signal intensities generated from f-AuNP coated cortex and the overlaid blue spectrum shows the background generated at the typical operating energy (6.5 μJ).



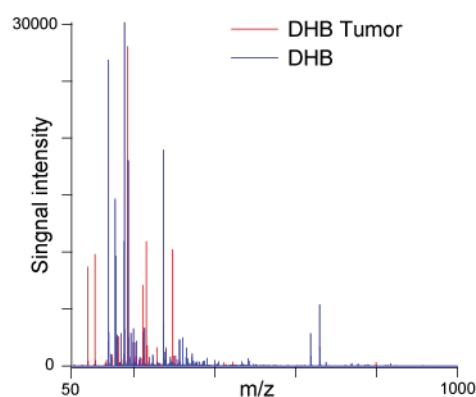
Supplementary Figure 11. Sinapinic acid background signal compared to tissue signal: mouse cerebral cortex. The red spectrum shows the signal intensities generated from f-AuNP coated cortex and the overlaid blue spectrum shows the background generated at the typical operating energy (6.5 μJ).



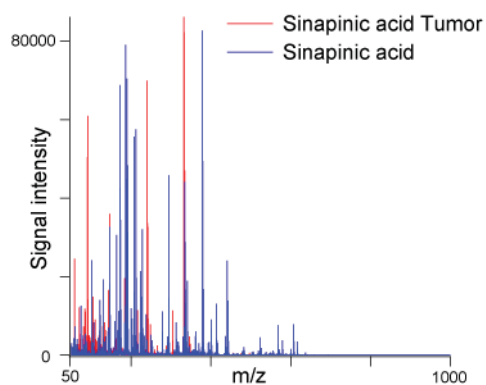
Supplementary Figure 12. F-AuNP background signal compared to tissue signal: mouse mammary tumor. The red spectrum shows the signal intensities generated from f-AuNP coated cortex and the overlaid blue spectrum shows the background generated at the typical operating energy (1.4 μJ).



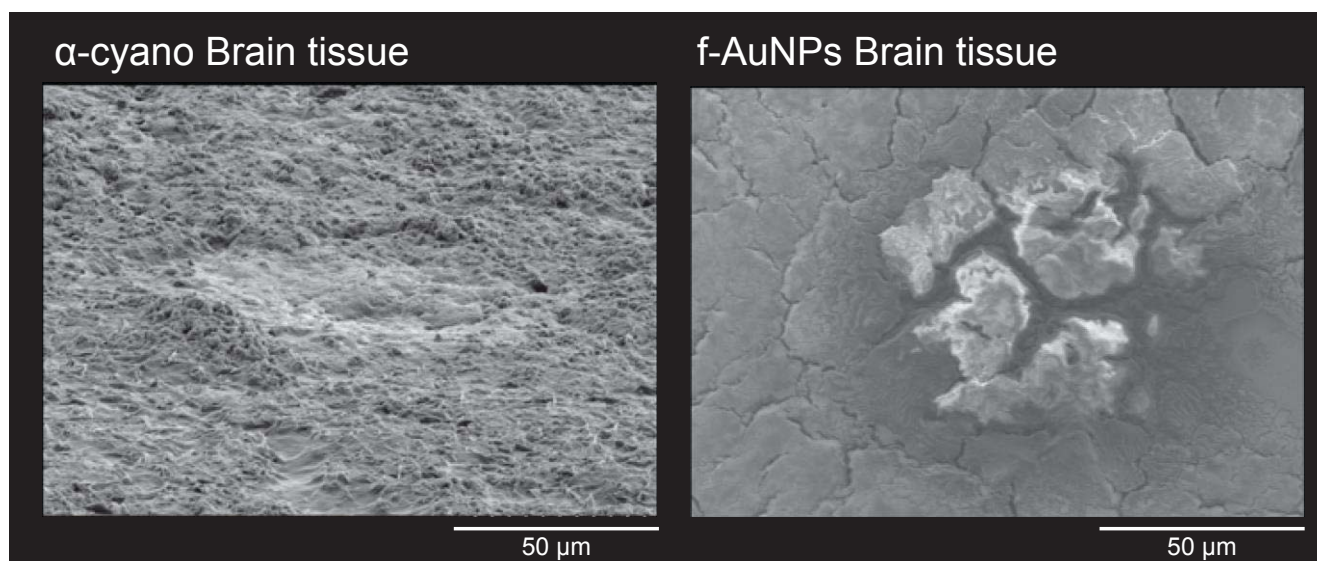
Supplementary Figure 13. α -cyano-4-hydroxycinnamic acid (α -cyano) background signal compared to tissue signal: mouse mammary tumor. The red spectrum shows the signal intensities generated from f-AuNP coated cortex and the overlaid blue spectrum shows the background generated at the typical operating energy (6.5 μ J).



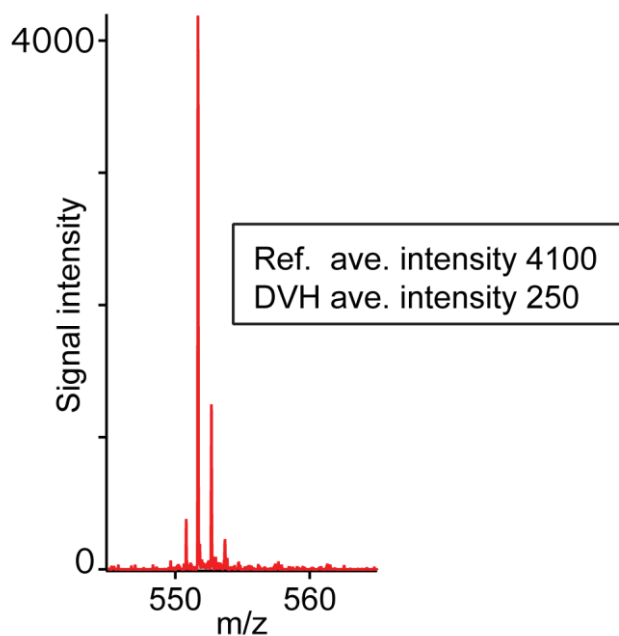
Supplementary Figure 14. 2,5-dihydroxybenzoic acid (DHB) background signal compared to tissue signal: mouse mammary tumor. The red spectrum shows the signal intensities generated from f-AuNP coated cortex and the overlaid blue spectrum shows the background generated at the typical operating energy (6.5 μ J).



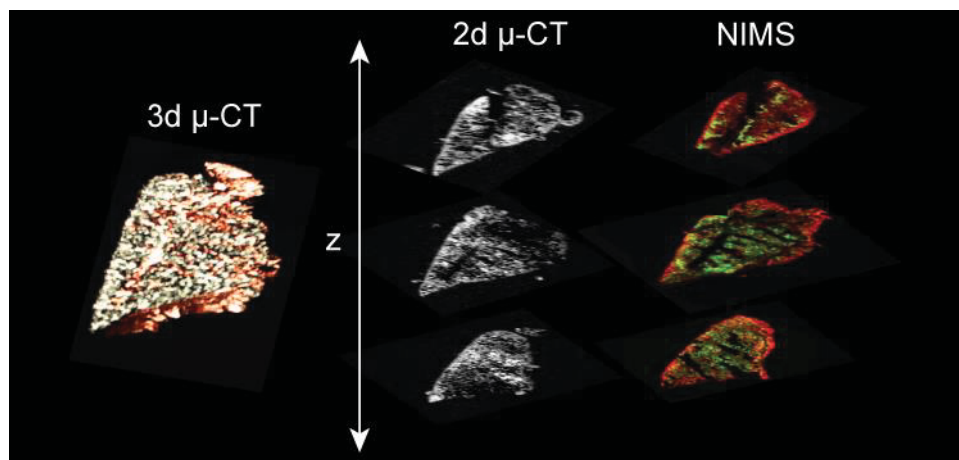
Supplementary Figure 15. Sinapinic acid background signal compared to tissue signal: mouse mammary tumor. The red spectrum shows the signal intensities generated from f-AuNP coated cortex and the overlaid blue spectrum shows the background generated at the typical operating energy (6.5 μ J).



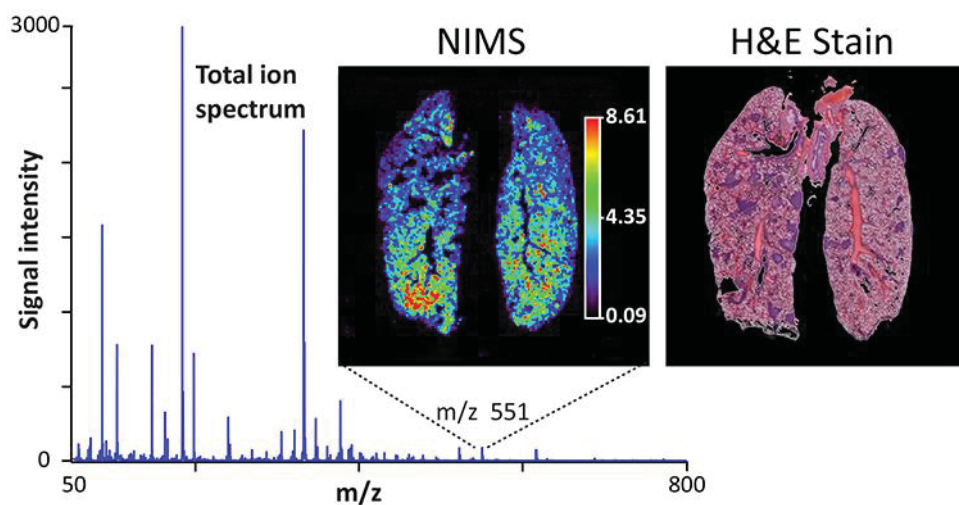
Supplementary Figure 16. Comparison of a crater observed following MALDI analysis of brain tissue using α -cyano-4-hydroxycinnamic acid (α -cyano) and a plateau created following NIMS analysis of brain tissue.



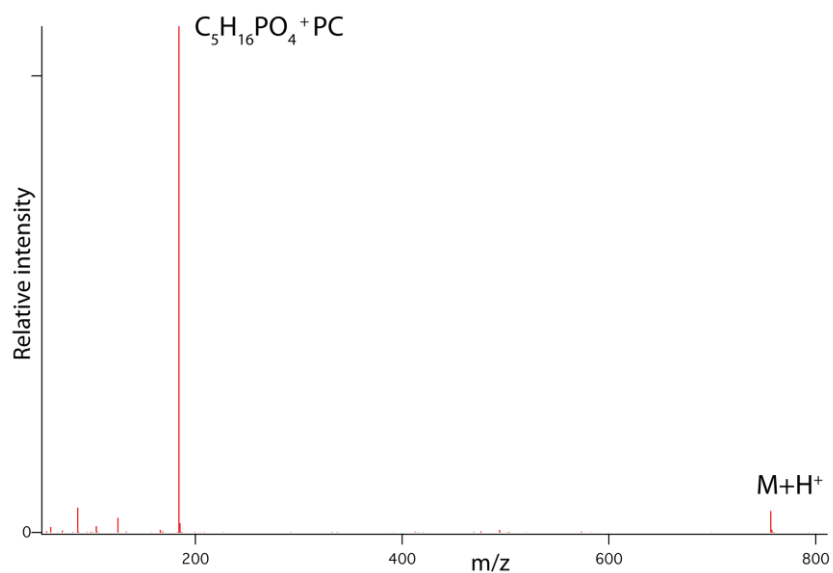
Supplementary Figure 17. NIMS spectrum of 100 μM DAG (16:0/16:0) $\text{M}+\text{H}-\text{OH}^+$ yielding approximately 20 times the signal measured in the bacteria.



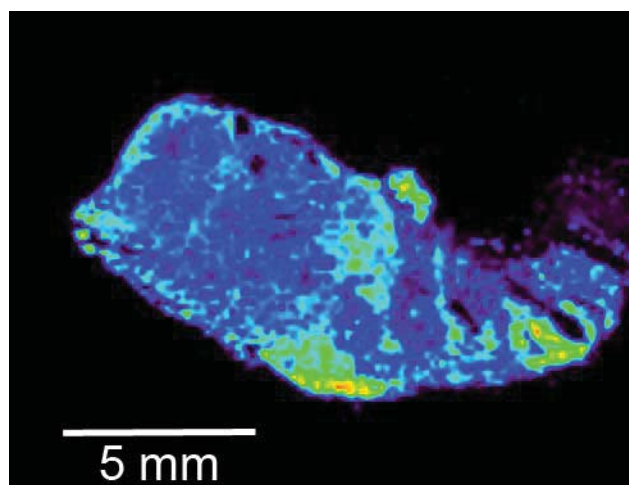
Supplementary Figure 18. 3D NIMS and μCT Imaging. A 3d surface projection of the left lobe of a f-AuNP ventilated mouse lung where the copper color indicates the surface whether it be at the exterior of the lung or a blood vessel in the interior of the lung silver indicates signal generated from the regions ventilated with the f-AuNPs. $\mu\text{-CT}$ images from 3 depths and positive ion NIMS images from 3 similar depths. The red pixels indicate the phosphocholine ion at m/z 184 and green pixels show the localization of m/z 551, which is most likely, a diglyceride ion.



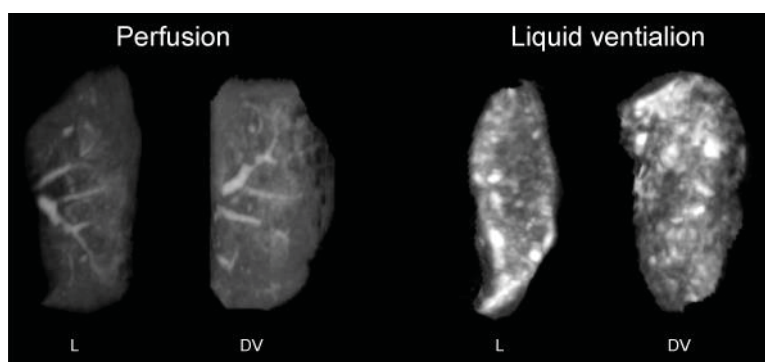
Supplementary Figure 19. NIMS and H&E stain of a metastatic mouse. Mass spectra generated from a metastatic mouse lung ventilated with f-AuNPs. The inset shows the ion image for m/z 551. The NIMS image is paired with an H&E stain of the same lung from approximately the same depth metastases appear as dark purple masses.



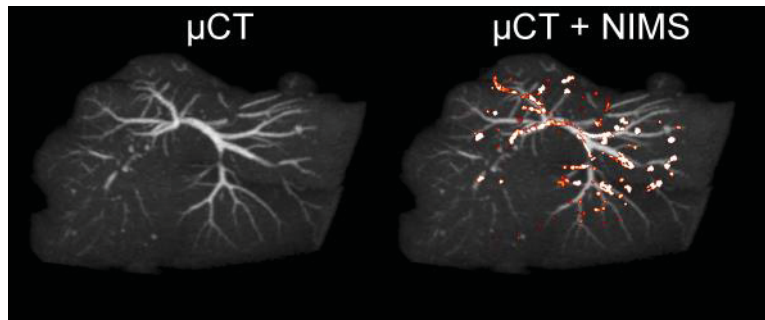
Supplementary Figure 20. Tandem mass spectrometry of m/z 756.5 found in mouse lung showing characteristic phosphocholine headgroup.



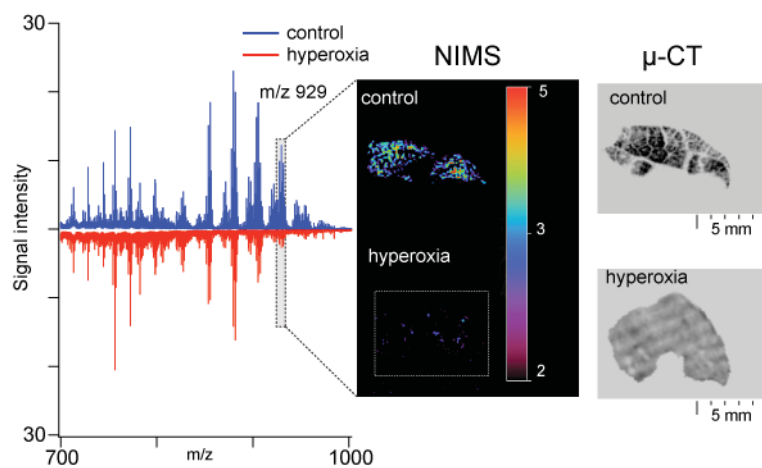
Supplementary Figure 21. NIMS image of a mouse mammary tumor that was coated with f-AuNP following sectioning. The ion mapped is phosphocholine at m/z 184.



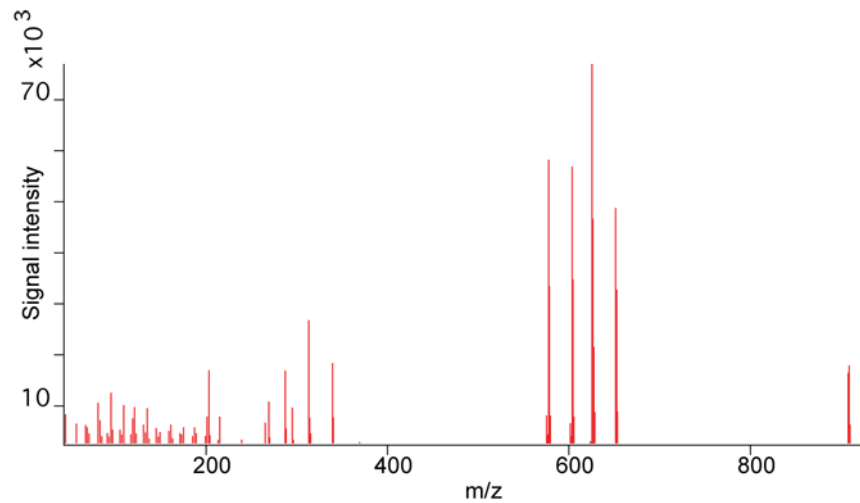
Supplementary Figure 22. A comparison between mouse lungs perfused and ventilated with f-AuNPs. A lateral and a Dorsal-Ventral μ CT view of a mouse lung perfused with f-AuNPs, compared to a lateral and a Dorsal-Ventral μ CT view of a mouse lung ventilated with f-AuNPs.



Supplementary Figure 23. A μ CT image of f-AuNP perfused mouse liver showing the 3-dimensional structure of the blood vessels and an overlay of a NIMS image of a 20 μ m section taken from the same tissue. The signal is only generated at the blood vessel surface where the nanoparticles have been perfused. The ion mapped is phosphocholine at m/z 184.



Supplementary Figure 24. NIMS and μ CT imaging using fluorinated gold nanoparticles. Mass spectra generated from two liquid ventilated mouse lung tissue slices; control (blue), hyperoxia conditions (red). The inset shows the ion image for m/z 929. Paired with these images are μ CT images of f-AuNP perfused lungs; control, hyperoxia at approximately the same depth. This ion was found to decrease on average by 66 ± 20 % ($n = 4$)



Supplementary Figure 25. Tandem mass spectrometry of the down regulated mass range in NIMS images of hyperoxia treated mouse lungs showing characteristic lipid fragment ions.

Supplementary Table

Supplementary Table 1. LC-MS/MS data for DAG (16:0/16:0) in balanced DVH compared to from MS/MS spectra for DAG (16:0/16:0) standards from Lipid maps. The common highest intensity fragment ion (313) is underlined and in bold.

MS/MS	Ref.MS/MS
551	551
<u>313</u>	<u>313</u>

Supplementary Discussion

Fluorinated AuNPs were employed to detect a variety of small molecules such as endogenous metabolites, drugs and peptides, as well as complex biological samples (e.g., plasma and bacteria extracts). Several examples of the use of fluorinated AuNPs in MS detection are demonstrated in **Supplementary Figure 1**. Verapamil, lysophosphatidylcholine (lysoPC), peptide bradykinin, and citric acid can be detected in nmol-fmol amounts using either positive or negative ionization modes with good signal to noise. The super-hydrophobic property of the fluorine surface creates an “anti-water” environment facilitating the protonation of the analyte. As shown in **Supplementary Figure 1**, and in contrast to typical particle desorption experiments, all the molecules are detected as protonated (i.e., $[M+H]^+$) or deprotonated peaks (i.e., $[M-H]^-$). Little or no cation adducts such as $[M+Na]^+$ or $[M-2H+Na]^-$ are observed.

Further, we also applied this technique to characterize complex biological samples (e.g., human plasma extracts), shown in **Supplementary Figure 2**. To effectively deconvolute the complexity of the human plasma samples, an ion mobility-MS technique is used for gas phase separation of desorbed ions and MS detection. There are at least two main ion mobility drift areas within the plasma sample. One is in the mass range 420-600 Da, the other one is with a mass range of 740-870 Da both are identified with a grey rectangle in Figure S1 and accompanied by the spectrum from each region. The ion mobility data and the mass range of the ions (m/z 740-870) are consistent with phospholipids in plasma. These experiments demonstrate multiple capabilities, the ability to use f-AuNPs to analyze complex biological samples, generate data consistent with literature results, its adaptability to ion mobility spectrometry, and different types of mass spectrometry instrumentation (TOF/TOF and QTOF).

The f-AuNPs generate very little background signal due to the low laser energies used in these experiments compared to other ligands known to insulate analyte from gold nanoparticles. For example optimal laser energies for LDI-MS with hexadecyltrimethyl-ammonium bromide (CTAB) functionalized AuNPs are selected based on a balance between signal intensity maximization and gold cluster

formation which coincides with fragmentation¹. **Supplementary Figure 3** compares the background spectra of the f-AuNPs at typical operation energy and the energy necessary to generate gold ion clusters. Here we show that optimal ion signal is obtained well below the threshold of gold cluster formation. Background signal for the f-AuNPs was also compared to three MALDI matrices: α -Cyano-4-hydroxycinnamic acid (α -Cyano), 2,5-dihydroxy benzoic acid (DHB), 3,5-dimethoxy-4-hydroxycinnamic acid (Sinapinic acid) across three types of tissue human saphenous vein (**Supplementary Figure 4-7**), mouse cerebral cortex (**Supplementary Figure 8-11**) and a mouse breast tumor (**Supplementary Figure 12-15**).

We also applied these imaging approaches to investigate the effects of hyperoxia on the lung tissue of juvenile mice. Research in the area of hyperoxia enhances our knowledge of the effects of oxygen toxicity, which are not well known even though it is used as a therapeutic by an estimated 800,000 patients each year in the US alone^{2-4 5 6}. It is known that the high oxygen levels lead to an excess of reactive oxygen species (ROS) affecting the pulmonary capillary endothelial and alveolar epithelial cells⁴ located near the surface of the lung tissue. Therefore the liquid ventilation method combined with NIMS and μ CT are particularly well suited for examining hyperoxia. For this experiment, a 7 day old mouse pup was exposed to hyperoxia conditions for 5 days. This model was originally developed to study retinopathy associated with the exposure of premature infants to hyperoxia conditions⁷. The exposed animal's lungs were ventilated with the f-AuNP solution and removed for analysis. As a control, an age matched (12 days old) mouse was also ventilated with the f-AuNPs. **Supplementary Figure 24** shows mass spectrometry imaging analysis of mouse lung tissue harvested from a control mouse and one under hyperoxia conditions. The mass spectra generated for the control and treated lung show unique spectral features indicating chemical differences in these tissues. Analyzing tissue areas within the same image allows us to compare relative amounts of each detected chemical⁸. The inset in **Supplementary Figure 24** shows the chemical map of the ion at m/z 929, indicating strong localization of this compound within the control tissue and weak localization in the

hyperoxia treated tissue. This was true for a range of masses between m/z 850 and 950 and this was replicated to ensure that the relative differences were reliable, for example m/z 929 was decreased by $66 \pm 20 \%$ ($n = 4$). The ions over this range are potentially triglycerides and phospholipids which are classes of lipids that are known to be reduced in the lung surfactant of animals upon acute alveolar injury⁹. The masses across this range were confirmed as lipid species using liquid chromatography MS-MS analysis of the tissue (**Supplementary Figure 25**). The μ CT images that are paired to the chemical images show that the hyperoxia treated lung has less apparent structural integrity, possibly indicating injuries sustained by the lungs during exposure to high oxygen.

Supplementary References

- 1 Hsieh, Y. T., Chen, W. T. & Chang, H. T. Detection of nucleoside monophosphates through surface-assisted laser desorption/ionization mass spectrometry using CTAB-adsorbed gold nanoparticles. *J. Chin. Chem. Soc-Taipei* **58**, 761-768, (2011).
- 2 Tibbles, P. M. & Edelsberg, J. S. Hyperbaric-oxygen therapy. *New Eng. J. Med.* **334**, 1642-1648, (1996).
- 3 Bitterman, H. Bench-to-bedside review: Oxygen as a drug. *Crit. Care* **13**, 1-8, (2009).
- 4 Mach, W. J., Thimmesch, A. R., Pierce, J. T. & Pierce, J. D. Consequences of hyperoxia and the toxicity of oxygen in the lung. *Nurs. Res. Prac.* **2011**, 1-7, (2011).
- 5 Kim, V., Benditt, J. O., Wise, R. A. & Sharafkhaneh, A. Oxygen therapy in chronic obstructive pulmonary disease. *Proc. Am. Thorac. Soc.* **5**, 513-518, (2008).
- 6 Hickey, S. An audit of oxygen therapy on a respiratory ward. *Br. J. Nurs.* **16**, 1132-1137, (2007).
- 7 Smith, L. E. *et al.* Oxygen-induced retinopathy in the mouse. *Investigative ophthalmology & visual science* **35**, 101-111, (1994).
- 8 Ostrowski, S. G., Kurczy, M. E., Roddy, T. P., Winograd, N. & Ewing, A. G. Secondary ion MS imaging to relatively quantify cholesterol in the membranes of individual cells from differentially treated populations. *Anal. Chem.* **79**, 3554-3560, (2007).
- 9 Liao, D. F., Barrett, C. R., Bell, A. & Ryan, S. F. Functional abnormalities of lung surfactant in experimental acute alveolar injury in the dog. *Am. Rev. Respir. Dis.* **136**, 395-401, (1987).